

Design of Airborne Radome Using Novel Temperature Dependent Electromagnetic Modeling

Aparna Parameswaran and Hrishikesh S. Sonaliker*

Abstract—In this paper, a novel temperature dependent electromagnetic modeling for the design of airborne radome is presented. A smooth spatial temperature distribution on the radome surface is modeled using a piecewise cubic hermite interpolating polynomial as well as piecewise linear interpolation. The temperature gradient across the radome wall is modeled using an inhomogeneous planar layer. The performance of a radome is computed using the 3D ray tracing method in conjunction with aperture integration. A unique radome wall configuration is obtained for each ray for the accurate representation of a hot radome. A streamlined radome designed using the proposed model shows a significant performance improvement over the radome designed at the average temperature. The designed radome has the minimum insertion loss of 0.015 dB and the maximum boresight error of 1.8 mrad. The proposed method can be easily used with the experimentally obtained temperature distribution to predict the changes in radome performance in changing hypersonic environment.

1. INTRODUCTION

Radome is a protective housing used for sheltering an antenna from harsh environmental conditions [1]. The materials preferred for radome construction should be transparent to the electromagnetic (EM) waves transmitted or received by the antenna [2]. In practice, radome contributes to the degradation of antenna performance by causing transmission loss. In airborne applications, the streamlined shape of the radome results in Bore Sight Error (BSE). Therefore, Power Transmission (PT) and BSE are the two important performance parameters of the radome. These performance parameters can be determined from radiation pattern of the antenna enclosed by the radome [3].

Due to the need for satisfying simultaneous electromagnetic and structural requirements, the design of streamlined airborne radomes is a very challenging task. The aim of the design is to maximize the PT and minimize the BSE while maintaining the structural integrity. A streamlined radome with graded variation of dielectric parameters across inhomogeneous radome wall was proposed in [4, 5] for realizing improved PT. An improvement in the BSE performance of an A-sandwich airborne radome was realized in [7]. Xu et al. proposed the use of particle swarm optimization and an innovative concept for determining the best wall thickness profile for airborne radomes [8, 9]. A detailed study on the design aspects of the constant and the variable thickness airborne radomes was presented in [10]. Improvement in the BSE performance of an airborne radome under circular polarization was studied in [11]. Although different effective design techniques were used in these and other works, the effect of temperature on radome EM performance was not considered.

In a hypersonic environment, the electrical properties of the radome material change due to heating of radome caused by atmospheric drag [12]. As a result, the PT and BSE values of the radome also deviate from their designed values. Kilcoyne's work was one of the earliest to discuss the numerical methods useful for the analysis of hot radome [13]. The work proposed a 2D ray tracing method for

Received 17 April 2020, Accepted 9 July 2020, Scheduled 23 July 2020

* Corresponding author: Hrishikesh Shashikant Sonaliker (hrishikeshs@goa.bits-pilani.ac.in).

The authors are with the Department of Electrical and Electronics Engineering, Goa Campus, BITS Pilani, India.

analyzing an ogive radome. The radome geometry was divided into different window regions to consider the effect of spatial temperature distribution. The radome wall section in each window consisted of different numbers of layers to represent nonlinear temperature gradient. Later, Weckesser et al. calculated the change incurred in the BSE of a missile radome because of the heating effects [14]. In this work, a von Karman radome with a multi-layer wall configuration and multi axial sections was subjected to an analytical study. Results of both these works suggested the need for developing better models for radome performance analysis at elevated temperatures.

Recently, the temperature dependent performance prediction of the dielectric slab modelled as an Inhomogeneous Planar Layer (IPL) was presented for applications in airborne radomes [15]. The temperature dependent EM analysis and design of a planar dielectric wall with an ablative layer was presented in [16, 17]. These works deal with planar radome wall and hence are limited in their application in practical scenarios. Nair et al. proposed a tangent ogive radome with an IPL wall configuration [18]. The spatial temperature distribution of this radome was characterized by dividing the radome in different EM window regions based on different antenna scan angle ranges. Each window had a constant inner and outer temperature. The results were computed separately for each window, and the adverse effects of discontinuous boundaries of two adjacent windows were not considered.

In this work, we propose a novel modeling of the hypersonic radome using a smooth variation of spatial temperature on the radome surface and IPL wall configuration. The use of a Piecewise Cubic Hermite Interpolating Polynomial (PCHIP) and a piecewise linear interpolation is explored to obtain an accurate spatial temperature distribution. The 3D ray tracing method based on geometrical optics and aperture integration is developed for the computation of radome EM performance parameters based on the new model. To make the work applicable in practical scenarios, the design of a tangent ogive 3D radome geometry is considered. The radome performance parameters computed with the proposed IPL models are compared with those computed with previously used models such as the Monolithic model and Window model. The results obtained show that the radomes designed using the proposed IPL models show significant improvement in the performance.

Section 2 presents the antenna radome configuration as well as the different radome models and numerical methods used in this work. Section 3 presents the PT, BSE, phase distribution, and antenna pattern results of the designed radomes. Section 4 presents a discussion and comparison with the previous literature. Finally, Section 5 presents a few concluding remarks.

2. RADOME MODELS AND NUMERICAL METHODS USED

2.1. The Antenna-Radome Configuration

In this work, a typical tangent-ogive radome having a length of 1 m and a base diameter of 0.5 m is considered [19]. Fig. 1 shows the antenna-radome configuration. The radome encloses an aperture antenna with a diameter of 0.2 m. The operating frequency of the antenna is 10 GHz. The antenna is assumed to be mounted on the EL/AZ type of gimbal with zero rotational offsets. The antenna is located at the distance of 0.3 m from the radome base. EM waves are assumed to originate from a rectangular grid of 112 source points located on the aperture. The source points are spaced half wavelength apart. The incident electric field at each source point is assumed to be linearly polarized along y' direction. The thickness of the radome wall is optimized to ensure the maximum power transmission at the highest angle of incidence. The average value of the dielectric constant and loss tangent of the material used for the radome wall are 5.7617 and 0.00261, respectively [20]. The electromagnetic performance of the radome is computed using different radome models which are described as follows.

2.2. The Monolithic Model

Monolithic Model is the simplest model used for the design of airborne radomes. In this model, a monolithic radome wall is specified by a single value of the dielectric constant (ϵ_r) and loss tangent ($\tan \delta$) corresponding to the material used for the wall. The value of the dielectric constant and the loss tangent in this model are usually specified either at the room temperature or at an average temperature of the radome wall. Therefore, this model cannot take into account the temperature gradient across the thickness of the radome wall. If the radome is designed using this model, then the performance of

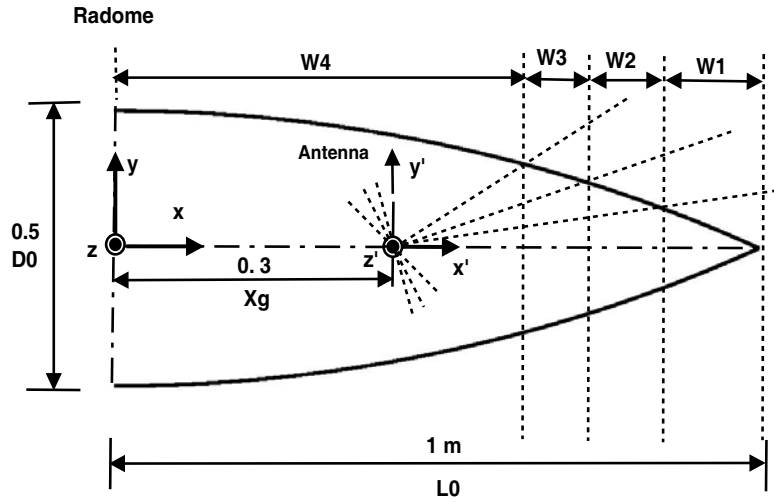


Figure 1. The antenna-radome configuration. (x', y', z') represent the antenna coordinate system and (x, y, z) represent the radome coordinate system. x - y is the elevation plane and x - z is the azimuth plane.

the radome may significantly deviate when the radome is operated at a different temperature. In this paper, the radome designed using the Monolithic model is called Monolithic radome.

2.3. The IPL Model

This is a novel Inhomogeneous Planar Layer (IPL) radome model proposed in this work. The purpose of the IPL model is to take into account the spatial temperature distribution on the surface of the radome and the temperature gradient across the radome wall for the design of airborne radomes. By using the IPL model, it is possible to optimize the radome performance for the hypersonic environment which produces a specified temperature distribution on the radome.

In the IPL model, first the temperatures on the inner and outer surfaces of the radome at different positions on the radome axis are obtained either experimentally or theoretically. Table 1 lists the values of the temperature at the inner and outer surfaces of the radome at 5 positions on the radome axis. It can be observed that the radome nose experiences higher temperature than the radome base. Also, the outer temperatures are higher than the inner temperatures. These values represent a typical scenario of the hypersonic environment used in this work [13]. Depending on the application, suitable temperature distribution data can be used.

Table 1. Spatial temperature distribution data points.

Position on radome axis (m)	Inner Temperature (F)	Outer Temperature (F)
0.00	100	250
0.45	200	575
0.75	300	900
0.95	900	1500
1.00	1000	1600

Once the temperature distribution data points are obtained, it is necessary to use a suitable interpolation method to compute the inner and outer temperatures of the radome wall at any given position on the radome axis. Fig. 2 shows the original temperature data points along with

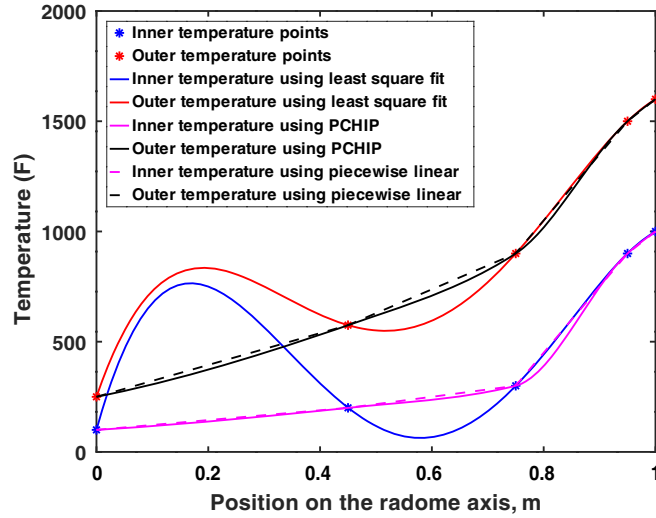


Figure 2. Interpolating polynomials showing change in the temperature as a function of the position on the radome axis.

the interpolated values computed using three different interpolation methods. It can be observed that the interpolating polynomials of degree 4 calculated using the least square fit method tend to oscillate between the data points and therefore not suitable. Piecewise linear method provides a good approximation of the temperature variation by placing a straight line between the two data points. Although it is a simple method, the first derivative of the approximation becomes discontinuous at the data points.

For the radome geometry considered, a practical temperature distribution on the radome surface is a smooth function of position having smoothly varying derivatives. Therefore, a method based on Hermite interpolation can be used to effectively model the temperature. The Piecewise Cubic Hermite Interpolating Polynomial (PCHIP) is a third degree piecewise polynomial function having shape preserving characteristics. In this technique, the first derivative of the polynomials in neighboring intervals is matched at the data points [21]. The general form of the PCHIP is given by

$$P_j(x) = a_{0,j} + a_{1,j}x + a_{2,j}x^2 + a_{3,j}x^3 \quad (1)$$

where coefficients $a_0 \dots a_3$ are computed for each interval j where $1 \leq j \leq n - 1$ using an inbuilt MATLAB function PCHIP. Fig. 2 shows that the interpolation using the PCHIP not only provides a smooth transition between the data points with continuous first derivative but also avoids unnecessary overshoots or undershoots.

Both the PCHIP and piecewise linear interpolation methods are used in this work. The IPL models using these two methods are named as IPL PCHIP model and IPL Linear model, respectively.

Figure 3 shows the EM waves (rays) originated from the antenna intercepting the radome wall at different points. Due to the presence of the spatial temperature distribution on the radome surface, each ray experiences a different inner and outer temperature at the point of interception with the radome wall. As a result, each ray experiences a different wall configuration. Once the x coordinate of the point of interception for each ray is computed, the inner and outer temperatures experienced by each ray can also be obtained using the piecewise linear or PCHIP interpolating functions previously calculated.

Once the inner and outer wall temperatures for the ray are obtained, the temperature gradient across the radome wall can be established. For simplicity, a linear variation of temperature between the inner and outer surfaces of the radome wall is considered in this work. The radome wall is then modelled as an inhomogeneous planar layer made of multiple layers, each layer at a different temperature [22]. The dielectric constant and loss tangent value of each constituent layer are computed by performing a polynomial fit on the temperature dependent material data as shown in Fig. 4 [23]. Our trials have shown that using 25 layers to model the radome wall is sufficient to ensure acceptably low error tolerance [24].

In this way, both the spatial temperature distribution on the radome surface and the temperature

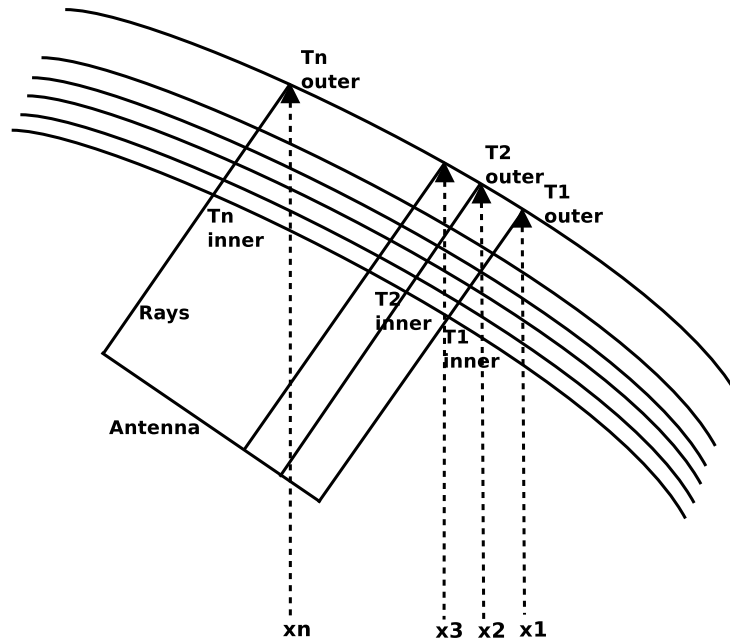


Figure 3. The spatial temperature distribution experienced by the EM waves passing through the radome in the IPL model.

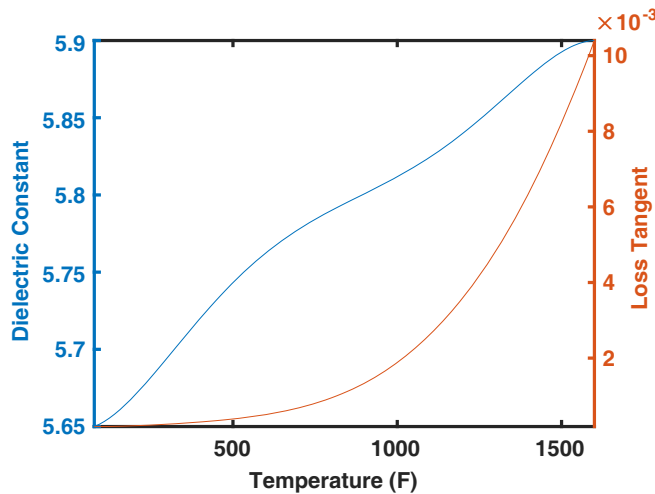


Figure 4. Polynomials showing variation of electrical parameters of the radome wall material with temperature.

gradient across the radome wall can be taken into account by the IPL model. The novelty of the IPL model presented here lies in obtaining the unique radome wall configuration for each of the rays intercepting the radome wall at a given antenna scan angle. In this paper, the radome designed using the IPL model is called as IPL radome.

2.4. The Window Model

For the purpose of comparison with the previous literature and completeness, in this work, the performance of the radome is also computed using the Window model. In the Window Model, the radome geometry is divided into different window regions based on antenna scan angle ranges. These window regions are represented as $W1$, $W2$, $W3$, and $W4$, respectively as shown in Fig. 1. The radome

Table 2. Spatial temperature distribution in the window model.

Window	Position on radome axis (m)	Antenna scan angle (deg)	Inner Temperature (F)	Outer Temperature (F)
<i>W1</i>	1.00–0.95	0.00–2.27	800	1550
<i>W2</i>	0.95–0.75	2.27–14.12	600	1200
<i>W3</i>	0.75–0.45	14.12–53.37	250	737.5
<i>W4</i>	0.45–0.00	53.37–90.00	150	412.5

wall portion in each window has a constant inner and outer temperatures. Table 2 lists the position of each window in this model. To make the Window model comparable to the IPL model, the inner and outer temperatures of the radome wall in each window are obtained from the same spatial temperature distribution data points listed in Table 1. It can be noted that window *W1* constitutes the nose section of the radome and experiences the highest inner and outer temperatures whereas *W4* constitutes the radome base region and experiences the lowest inner and outer temperatures. Similar to the IPL model, the window model also considers a linear temperature gradient between the inner and outer surfaces of the radome wall. All the rays emanating from the antenna and intercepting the radome wall in the same window region experience the same wall configuration. In this paper, the radome designed using the Window model is called as the Window radome.

2.5. The 3D-Ray Tracing Procedure

One of the challenges in the analysis and design of airborne radomes is the selection of method to accurately model the antenna and radome as a system. An excellent review of such methods is provided in [6]. These methods can be grouped into the following categories. The Method of Moments (MoM), Finite Element Method (FEM), and Finite Difference Time Domain (FDTD) method are examples of full wave low frequency methods. Although they are more accurate, their use is limited to electrically small radomes as they require huge computational resources. Ray tracing methods based on geometrical optics (GO) or physical optics (PO) are examples of high frequency methods suitable for electrically large radomes. Although they are computationally efficient, they are relatively less accurate as they use flat panel approximation at the point of intersection of the ray with the radome wall. Hybrid methods such PO-MoM are also proposed in order to combine the advantages of low and high frequency methods. In this work, the 3D ray tracing procedure based on geometrical ray optics in transmitting mode is used to compute the radome performance parameters such as power transmission (PT) and boresight error (BSE). This method can be conveniently implemented on personal computers and gives accurate results when the dimensions of the antenna are five wavelengths or higher [7].

The ray tracing procedure starts by transforming the coordinates of source points on the antenna aperture from the antenna coordinate system to the radome coordinate system (Fig. 1). This coordinate transformation takes into account the gimbal rotations in the azimuth and elevation planes. Due to a relatively small effect of gimbal offsets on radome performance parameters, the values of elevation and azimuth gimbal offsets are set to zero [25]. Then, the rays are traced from each source point to the radome wall, and the point of interception of rays with the radome wall is determined. At each interception point, the angle of incidence of the ray is calculated. Then, depending on the radome wall configuration, the angle of incidence, and the polarization of incident electric field, the complex transmission coefficient for each ray is computed. Finally, the antenna sum pattern is obtained by the aperture integration method as [3],

$$S = \frac{\sum_{i=1}^M F_a e^{-j \sin \theta (y_i \cos \phi + z_i \sin \phi)} T_i}{\sum_{i=1}^M F_a}. \quad (2)$$

Here, M represents the number of source points and the number of rays originating from these source points. T_i is the transmission coefficient for i th ray, with (y_i, z_i) being the coordinates of the i th source point in the antenna coordinate system. θ and ϕ are the angles in the antenna space. F_a is the uniform aperture field distribution.

Once the antenna sum pattern is obtained, the power transmission and boresight error is given by [8],

$$\text{PT} = 20 \log_{10}(|S_{\text{peak}}|) \quad (3)$$

$$\text{BSE} = \text{angle}(|S_{\text{peak}}|), \quad (4)$$

respectively. Here, $|S_{\text{peak}}|$ is the numerically determined peak of the sum pattern, and the term ‘angle’ means the angular location of the sum pattern peak.

The 3D ray tracing procedure can be directly applied to the Monolithic model of the radome. In the case of the Window model, the rays are first categorized into different window regions depending on their point of interception on the radome wall. Each window has a different wall configuration depending on the inner and outer temperatures of that window. The wall configuration of a particular window is used for the rays falling within that window. In the case of the IPL model, each ray experiences a different radome wall configuration. The wall configuration of a particular ray is computed from the inner and outer temperatures of the wall at the point of interception of that ray on the radome wall. As a result, the 3D ray tracing procedure is modified for different radome models considered in this work. The MATLAB code is newly developed to implement this procedure. The verification of the 3D ray tracing code is provided in Appendix A.

3. RESULTS

Table 3 shows the optimized radome wall thickness computed using different radome models. The optimum value of the wall thickness is computed by ensuring the maximum power transmission at the antenna scan position which causes the maximum angle of incidence. For the Monolithic model, the average values of the dielectric constant and loss tangent are used. For the IPL and Window models, the temperature distributions described in Sections 2.3 and 2.4, respectively, are used. It can be observed that the optimum thickness for the IPL radomes and Window radome is less than that for the Monolithic radome. Also, only a slight difference in the optimum thickness is observed for the two IPL radomes.

Table 3. Radome wall thickness optimized using different models.

Radome model	Optimized wall thickness (mm)
Monolithic	6.7533
IPL Linear	6.7079
IPL PCHIP	6.7073
Window	6.7264

3.1. Performance of the Radome Designed Using the Monolithic Model

Airborne radomes are often designed using the Monolithic model at either the room temperature or the average operating temperature. When such a radome is operated in the hypersonic environment, the deviation in the radome performance is expected. In order to understand the significance of these deviations, the performance of the radome designed using the Monolithic model is studied using the IPL and Window models.

Figures 5(a) and 5(b) show the co-polar and cross-polar power transmission performances of the radome designed using the Monolithic model, respectively. It can be observed that at the antenna scan angles higher than 10° , the co-polar power transmission of the IPL model and Window model is significantly higher than that of the Monolithic model. Similarly, the IPL and Window models have

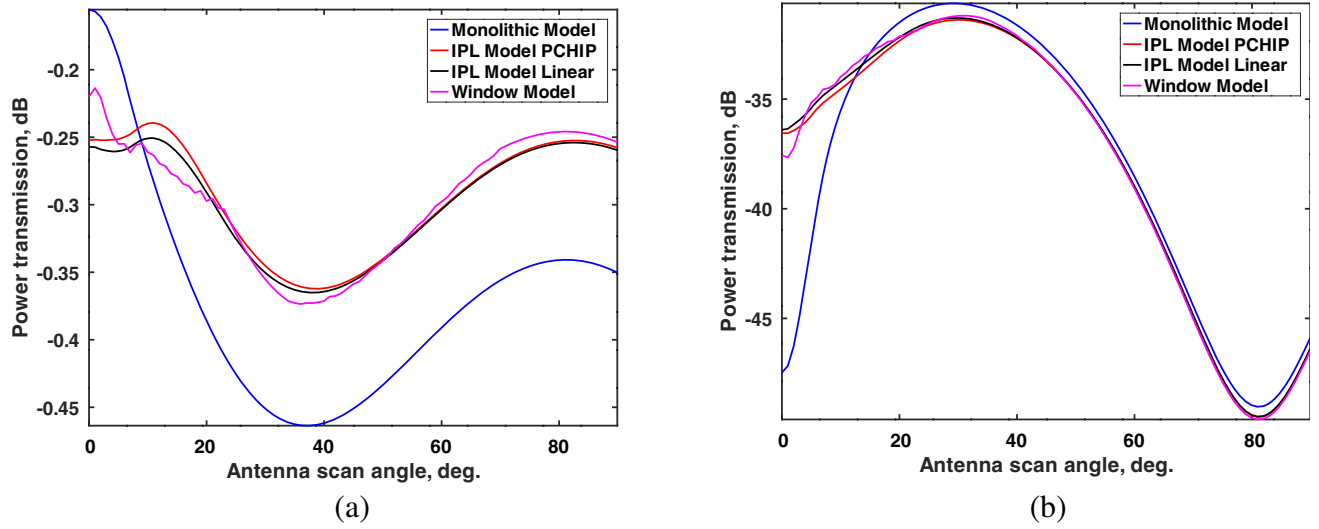


Figure 5. (a) The co-polar and (b) the cross-polar power transmission of the radome designed using the Monolithic model.

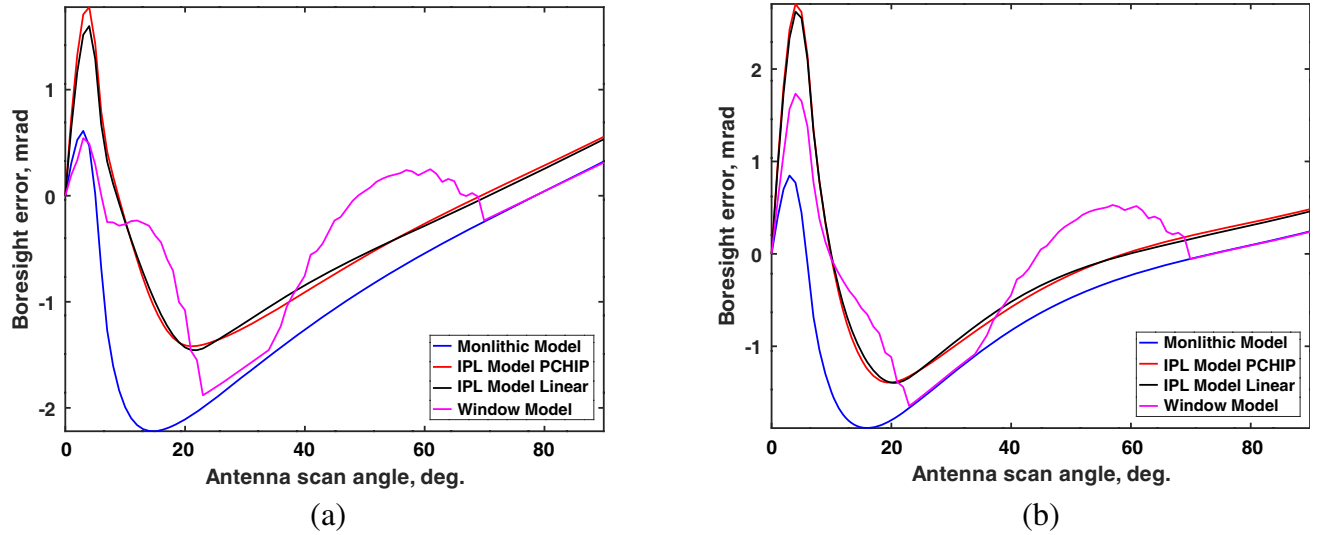


Figure 6. Boresight error performance of the radome designed using the Monolithic model in (a) the azimuth plane and (b) the elevation plane.

a slightly lower cross-polar power transmission than the Monolithic model at the higher antenna scan angles. Only near the radome nose, the power transmission of the Monolithic model is superior. As the radome was originally designed using the Monolithic model, this surprising result shows that the power transmission performance of the radome improves at the elevated temperatures.

Figures 6(a) and 6(b) show the boresight error (BSE) performance of the radome designed using the Monolithic model in the azimuth and elevation planes, respectively. It can be observed that when the antenna scan angle is less than 10° , the BSE of the Monolithic model is lower than that of the IPL and Window models. However, at the higher antenna scan angles, the BSE performance of the IPL model is significantly better than that of the Monolithic model. This result also suggests that the BSE performance of the Monolithic radome improves when it is analyzed at elevated temperatures. It is also important to note that the Window model exhibits sudden discontinuities in variation of BSE in both the planes. These discontinuities are in the antenna scan angle range from 10° to 25° as well as from

35° to 75°. The sudden and suspicious discontinuities in BSE predicted by the Window model suggest that this model may not be reliable for the computation of BSE, and the model needs to be scrutinized further.

3.2. Performance of the Radome Designed Using the IPL Model

The results shown in Figs. 5 and 6 show that although the radome was originally designed using the Monolithic model, the performance of the radome is seen to be improved when being analyzed using the IPL model. This result suggests that there is a possibility of improving the performance of the radome if it is designed using the IPL model.

Figures 7(a) and 7(b) show the co-polar and cross-polar power transmission performances of the radome designed using the IPL model, respectively. For the comparison, the performance of the radome designed using the Monolithic model is also shown. It can be observed that the co-polar power transmission of the IPL radome is significantly better than that of the Monolithic radome. The co-polar power transmission of the IPL radome is higher than -0.3 dB for the entire range of the antenna scan angles with the maximum value of -0.12 dB. Compared to the Monolithic radome, an improvement of 1.5 dB has been achieved. Also, the cross-polar power transmission of the IPL radome is significantly lower than that of the Monolithic radome. At 30° antenna scan angle, an improvement close to 5 dB is achieved over the Monolithic radome. The lower limit of the antenna scan angle, after which the IPL radome has a better performance than the Monolithic radome, is also reduced from 10° to 5° by designing the radome using the IPL model. It can also be noted that the power transmission performances of both the IPL PCHIP and IPL Linear radomes are better than the Window radome.

Figures 8(a) and 8(b) show the boresight error performance of the radome designed using the IPL model in the azimuth and elevation planes, respectively. It can be observed that at the antenna scan angles higher than 10°, the BSE of the IPL radome is significantly lower than that of the Monolithic radome. On the other hand, at the lower antenna scan angles, the Monolithic radome predicts lower BSE. However, from 10° to 90° scan angle range, the BSE of the IPL radome is less than 1.5 mrad. As a result, the improvement of 0.5 mrad has been achieved over the Monolithic radome. BSE performance of the Window radome is similar to that of the Monolithic radome except for the sudden discontinuities.

Table 4 shows the comparison of the radome performance parameters of the Monolithic radome and the IPL radome computed using the IPL PCHIP model. It can be observed that although the thickness of the IPL radome wall is only slightly different from that of the Monolithic radome, there can be a significant change in the power transmission and boresight error. These changes can also be observed by comparing Figs. 5 and 6 with Figs. 7 and 8, respectively.

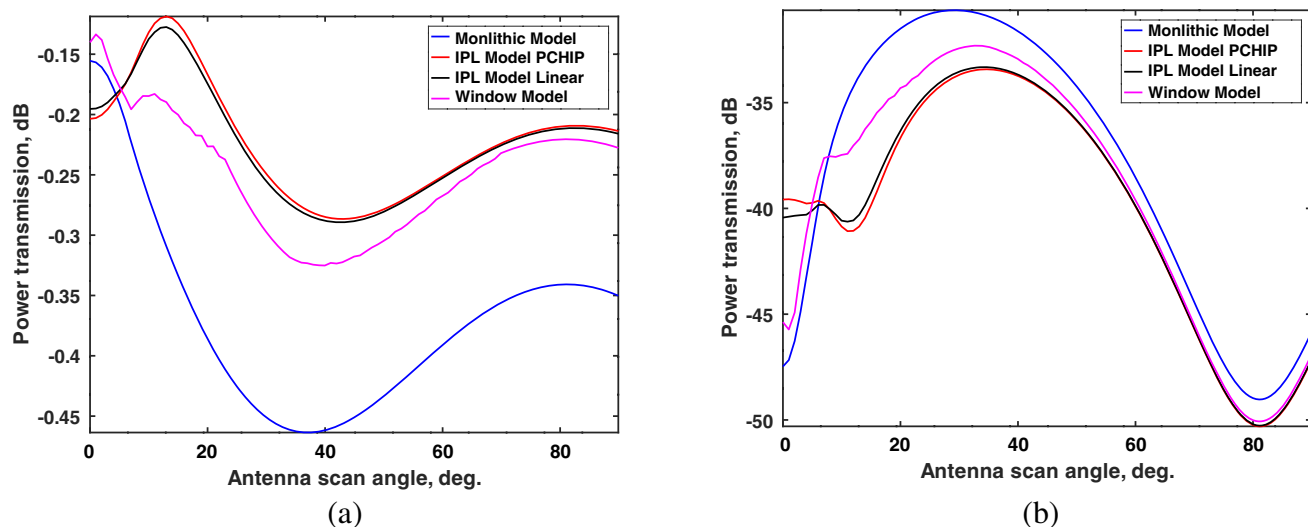


Figure 7. (a) The co-polar and (b) the cross-polar power transmission of the radome designed using the IPL model.

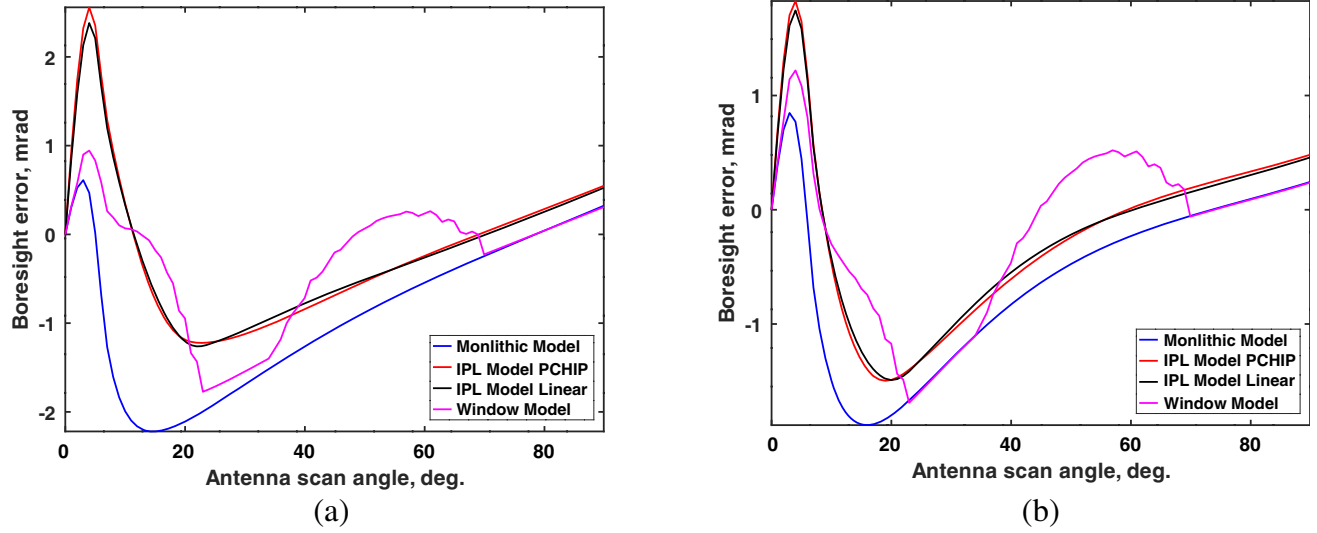


Figure 8. Bore sight error performance of the radome designed using the IPL model in (a) the azimuth plane and (b) the elevation plane.

Table 4. Comparison of the Monolithic radome and the IPL radome using the IPL model.

Radome wall thickness (mm)	Power transmission (dB)		Bore sight error (mrad)			
	Co-pol max	Cross-pol max	AZ max	AZ min	EL max	EL min
6.7533 (Monolithic)	-0.23	-31.384	1.7	-1.4	2.7	-1.3
6.7073 (IPL)	-0.1	-33.4	2.5	-1.2	1.8	-1.4

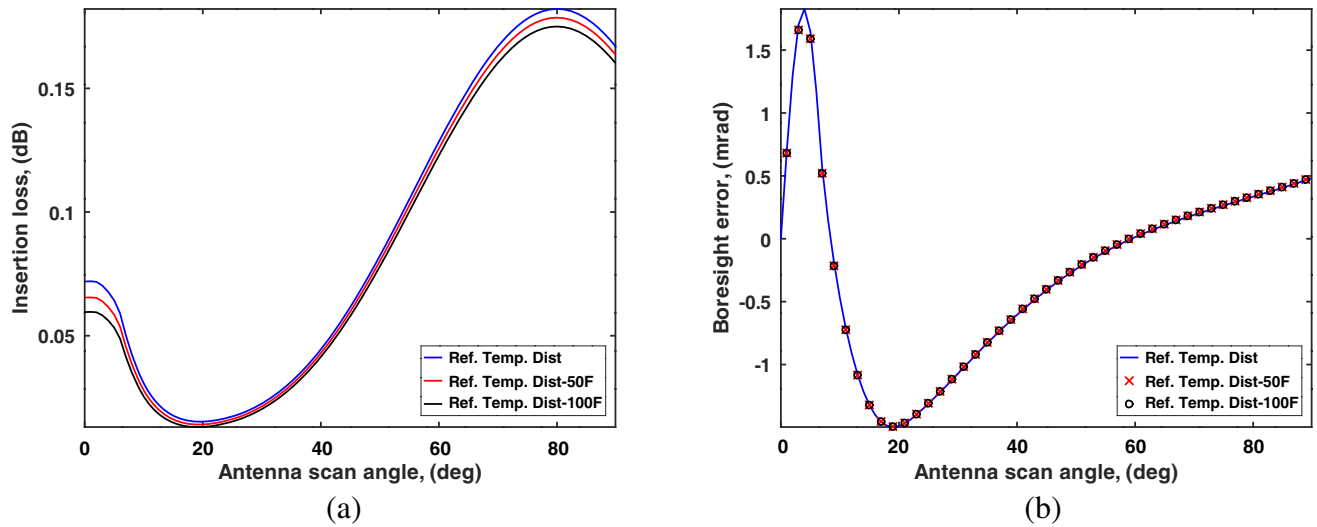


Figure 9. Change in (a) insertion loss and (b) bore sight error of the IPL radome due to variations in the surface temperature.

Although the optimum wall thickness of the IPL radome is computed for a specified temperature distribution on the radome surface, there may be variations in the temperature during the operation of the antenna-radome system. In order to observe how the radome responds to the changes in the temperature, the performance of the IPL radome is computed by reducing the temperature of the outer surface of the radome. Figs. 9(a) and 9(b) show the insertion loss and BSE performance of the radome at three different surface temperature distributions. A slight reduction in the insertion loss can be observed at the reduced temperature. On the other hand, there is no noticeable change in the BSE performance.

These results show that the performance of the radome can be significantly improved using the IPL model. It can also be noted that the IPL PCHIP model shows a marginally better performance than the IPL Linear model.

3.3. Aperture Phase Distribution and Antenna Patterns

To further investigate the reason behind the sudden discontinuities in the BSE predicted by the Window model, the aperture phase distribution and antenna sum patterns are computed at the selected antenna scan angles. The antenna scan angle values 15° , 52° , and 85° are chosen for this computation. 15° and 52° are chosen approximately in the middle of antenna scan angle ranges of 10° to 25° and 35° to 75° where the Window model predicts erroneous BSE. 85° is chosen where there is no erroneous prediction of BSE by the Window model.

Figure 10 shows the aperture phase distribution for different radome models at the chosen antenna scan angles in the azimuth plane. It can be observed that at 15° and 52° , the Window model has two distinct phase regions separated by a vertical line. This is because at 15° , some of the rays from the aperture fall in $W2$, and the rest of them fall in $W3$. Similarly at 52° , the rays are distributed between $W3$ and $W4$. As different windows have different temperature distributions, the rays in different windows experience abruptly different phase delays. This results in a significant shift of the antenna sum pattern of the Window radome as shown in Fig. 11. This shift in the sum pattern peak results in a sudden change in the BSE as long as the boundary between the two windows remains in the view of the aperture.

Figure 12 shows the aperture phase distribution for different radome models at the chosen antenna scan angles in the elevation plane. It can be observed that the phase distribution in the elevation plane

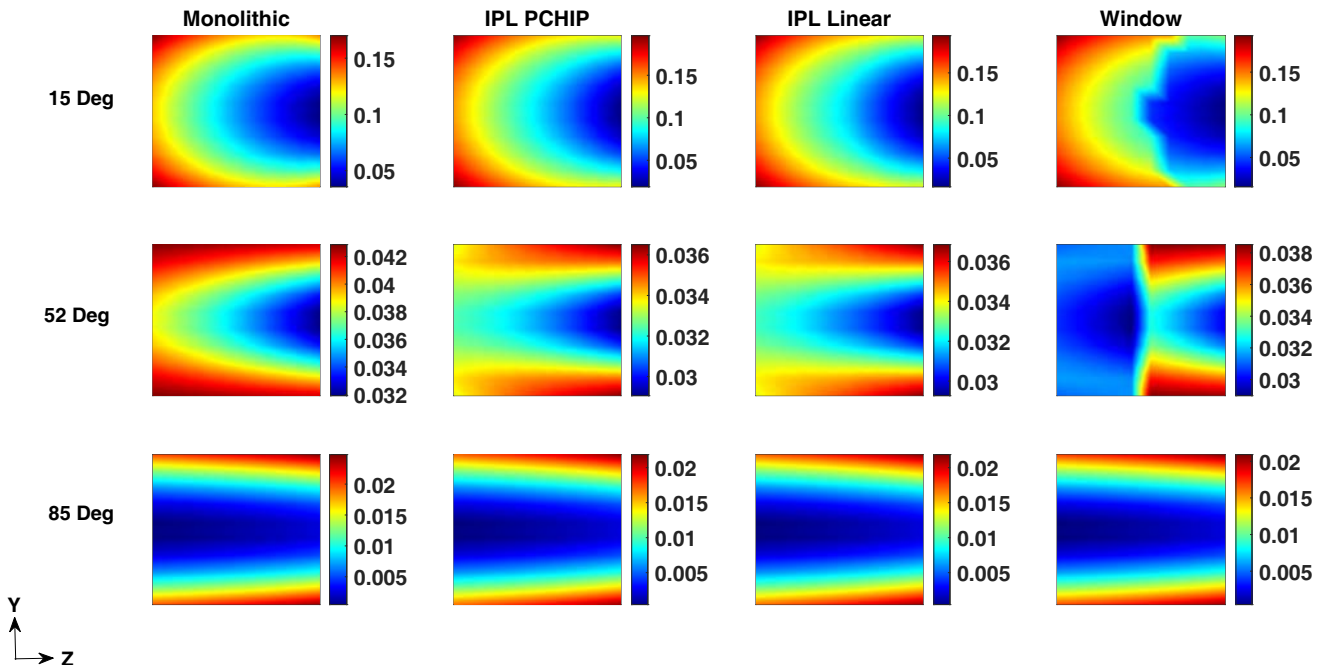


Figure 10. Aperture phase distribution at different antenna scan angles in the azimuth plane.

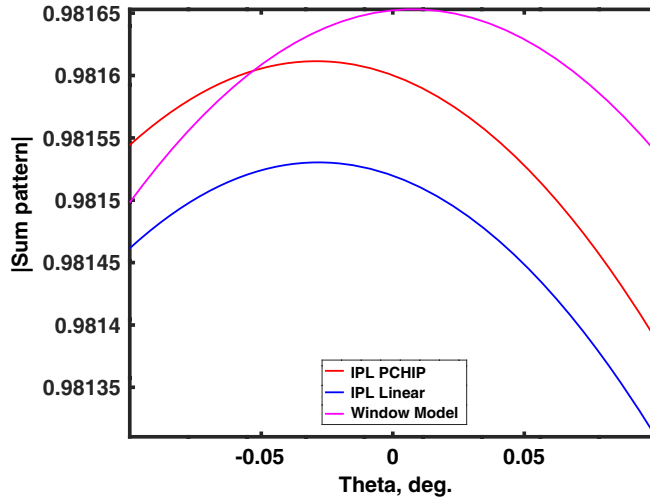


Figure 11. The antenna sum pattern at 52° scan angle in the azimuth plane.

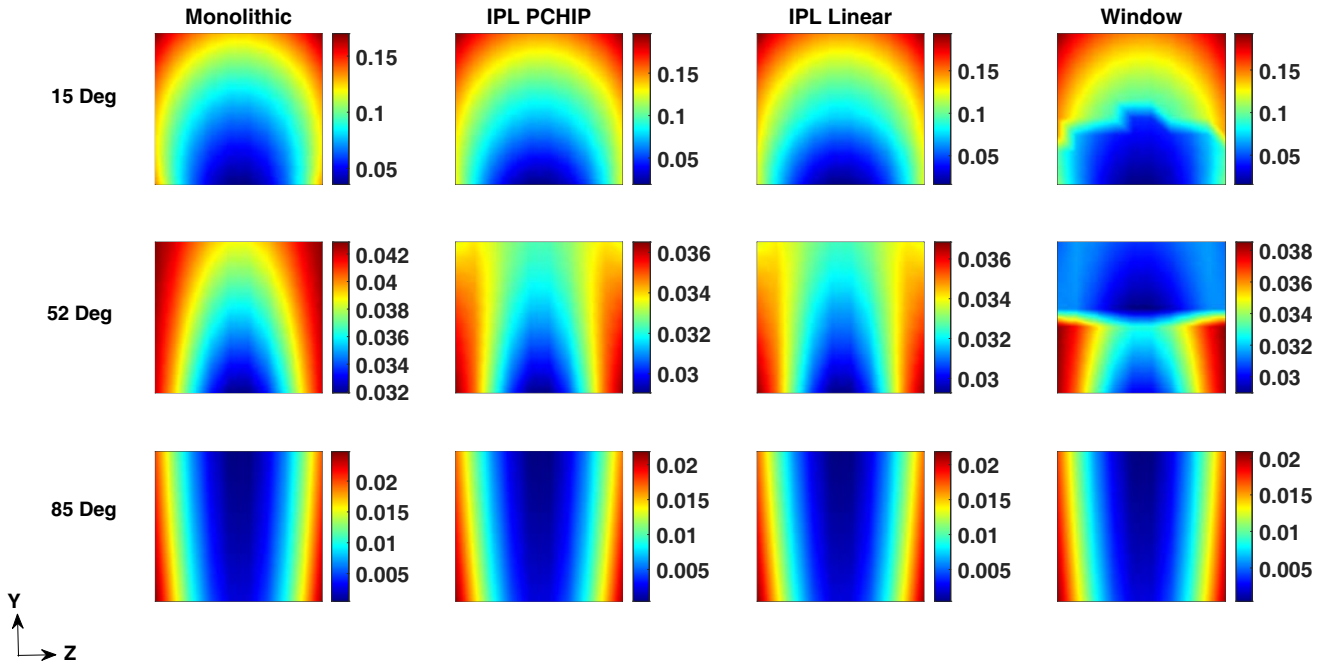


Figure 12. Aperture phase distribution at different antenna scan angles in the elevation plane.

is similar to that of the azimuth plane but oriented by 90°. In the elevation plane also, the Window model shows abrupt changes in phase due to distribution of rays in different windows at 15° and 52° scan angles. This results in shift of the antenna sum pattern peak location as shown in Fig. 13 and causes sudden changes in the BSE of the Window radome.

Due to the difference in the polarization of incident waves, the magnitudes of sum pattern peaks are different in the azimuth and elevation planes. Additionally, it can be observed that the magnitude of the sum pattern peak of the IPL PCHIP model is higher than that of the IPL Linear model in both the planes. This results in a better power transmission through the IPL PCHIP radome than the IPL Linear radome. At 85° scan angle, all the rays fall within $W4$ of the Window model. As a result, the four radome models show a similar phase distribution and a similar variation in BSE at the higher values of the antenna scan angle.

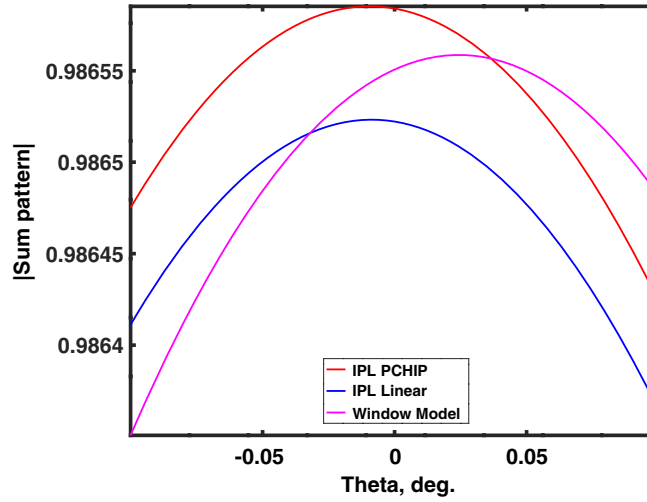


Figure 13. The antenna sum pattern at 52° scan angle in the elevation plane.

3.4. Computational Efficiency of Different Radome Models

Table 5 shows the computation time required to calculate the PT and BSE of different radomes using the 3D ray tracing method on Intel CORE i5 platform. The PT and BSE are computed at 90 different values of the antenna scan angle. The table also lists the number of ϵ_r and $\tan \delta$ values required to specify the radome wall configuration in each of the models. Due to a single layer wall configuration, the monolithic model requires the least computation time. The IPL model requires the most computation time as the wall configuration is separately obtained for each ray at every antenna scan angle. The IPL model using the PCHIP interpolation takes a slightly longer time than that using the piecewise linear interpolation. The Window model requires more computation time and memory than the monolithic model but less than that of the IPL models.

Table 5. Comparison of computational efficiencies of different radome models.

Radome model	Computation time (s)	ϵ_r and $\tan \delta$ values stored	
		General	Specific
Monolithic	31.9520	nLayers	1
Window	40.3142	nWindows * nLayers	$4 * 25 = 100$
IPL Linear	65.1503	nRays * nLayers	$112 * 25 = 2800$
IPL PCHIP	67.1622	nRays * nLayers	$112 * 25 = 2800$

4. DISCUSSION

The results obtained in this work show that the Monolithic model underestimates the influence of temperature on the radome performance. The Window model shows abrupt changes in phase and BSE due to discontinuous temperature values at the boundaries between two windows. The IPL model overcomes these limitations and can be effectively used to improve the radome performance without greatly increasing the computation cost.

Table 6 compares the radome modeling proposed in this work with the methods presented in the previous literature. The numbers in parentheses indicate the number of layers used in the IPL model of the radome wall or the number of windows used for spatial temperature distribution. Term EQ TLM means the equivalent transmission line method. It can be noted that the proposed IPL model is competitive in terms of modeling of the radome wall using the IPL. The proposed IPL model is superior

Table 6. Radome modeling proposed in this work in comparison with the previous literature.

Reference	Radome geometry	Modeling of radome wall	Modeling of spatial temperature distribution	Numerical method used
[15]	Planar	IPL (6)	-	EQ TLM
[16]	Planar	IPL (10)	-	EQ TLM
[17]	Planar	IPL (25)	-	EQ TLM
[13]	Ogive with cap	Analytical	Window (4)	2D ray tracing
[14]	Von Karman	IPL (9)	Window (12)	-
[18]	Tangent ogive	IPL (16)	Window (3)	3D ray tracing
Proposed work	Tangent ogive	IPL (25)	PCHIP and piecewise linear interpolation	3D ray tracing

Table 7. Performance comparison of the IPL radome design with the published literature.

Reference	Insertion Loss	Co-pol PT (dB)		Cross-pol PT (dB)		BSE Magnitude	Type of
	Min (dB)	Max	Min	Max	Min	Max (mrad)	Radome
[4]	-	-0.1	-0.5	-	-	2.5	CTR
[5]	-	-0.1	-0.45	-30	-68	2.3	CTR
[7]	-	-0.5	-1.5	-25	-50	3.8	CTR
[8]	0.375	-	-	-	-	0.5445	VTR
[18]	-	-0.18	-0.21	-37	-40	1.9	CTR
IPL PCHIP	0.015	-0.1	-0.28	-33.4	-50.3	1.8	CTR
IPL Linear	0.016	-0.12	-0.28	-33.3	-50.2	1.7	CTR

to the other works in terms of modeling an accurate spatial temperature distribution on the radome surface.

Table 7 compares the performance of the IPL radome designs proposed here with the previous literature. It is clear that the proposed designs exhibit a superior BSE performance to the CTR radome designs proposed in [4, 5, 7, 18]. The maximum value of co-polar PT of the proposed designs is the highest. The minimum value of the cross-polar PT of the proposed designs is lower than other designs except the one in [5]. Additionally, the PT of the proposed designs is better than the variable thickness radome presented in [8].

In hypersonic environment, the temperature also affects the radome geometry [26]. The loads incurred by the movement of airborne vehicle together with the variation in airflow and pressure during flight can alter the stress imposed on the radome structure. This stress is further worsened by aerodynamic heating. These factors affect the structural integrity of airborne radomes and cause deformations. Moreover, as the temperatures experienced at different parts of the radome are different, radome undergoes uneven thermal expansion, and the geometry of the radome is distorted. These effects are not considered in this work as they require a more extensive mathematical modeling.

5. CONCLUSION

In this paper, the design of the airborne radome using a novel temperature dependent electromagnetic modeling is presented. The spatial temperature distribution on the radome surface is obtained using a limited number of original data points and the PCHIP as well as the piecewise linear interpolation techniques. The temperature gradient across the radome wall is modelled using an inhomogeneous planar layer. The unique radome wall construction is obtained for each ray separately for realistic

analysis and design using the 3D ray tracing method. The utility of this approach is demonstrated by designing a radome which has the minimum insertion loss of 0.015 dB and the maximum boresight error of 1.8 mrad. The radomes designed using the novel IPL models have a significantly superior performance to the radome designed at the average temperature using the Monolithic model. The experimental study of radomes in high temperature hypersonic environment is very challenging, costly, and sometimes risky due to the use of rockets in the sled tests. The IPL models proposed in this work can be utilized to predict the deviations in radome performance in changing hypersonic environment. Also, the proposed approach can be easily generalized to work with the spatial temperature distribution data obtained using wind tunnel experiments and a suitable interpolation technique.

APPENDIX A. VERIFICATION OF 3D RAY TRACING METHOD

In this work, the in-house MATLAB based software library was developed to calculate the radome EM performance parameters. Preliminary checks were performed at every stage of software development. To further validate the accuracy of the program, the Constant Thickness Radome (CTR) geometry specified in [10] was selected as the simulation object. This radome has the base diameter of 0.5 m and height of 1 m. The radome encloses a linearly polarized antenna having diameter of 0.22 m with uniformly distributed aperture field. The frequency of operation is 9.4 GHz. The antenna is located at a distance of 0.3 m from the radome base. Radome wall is made of a glass composite with relative permittivity of 4 and loss tangent of 0.015 and has the thickness of 8.98 mm. An additional 0.2 mm thick layer of radome paint with relative permittivity of 3.46 and loss tangent of 0.068 is also presented. Figs. A1(a) and A1(b) show the transmission loss and boresight error of CTR computed by our 3D ray tracing code. The y axis ranges of these figures are adjusted to match those in [10]. This result is identical to the transmission loss and boresight error performance presented in Fig. 7 of [10] and indicates that the 3D ray tracing code provides accurate results.

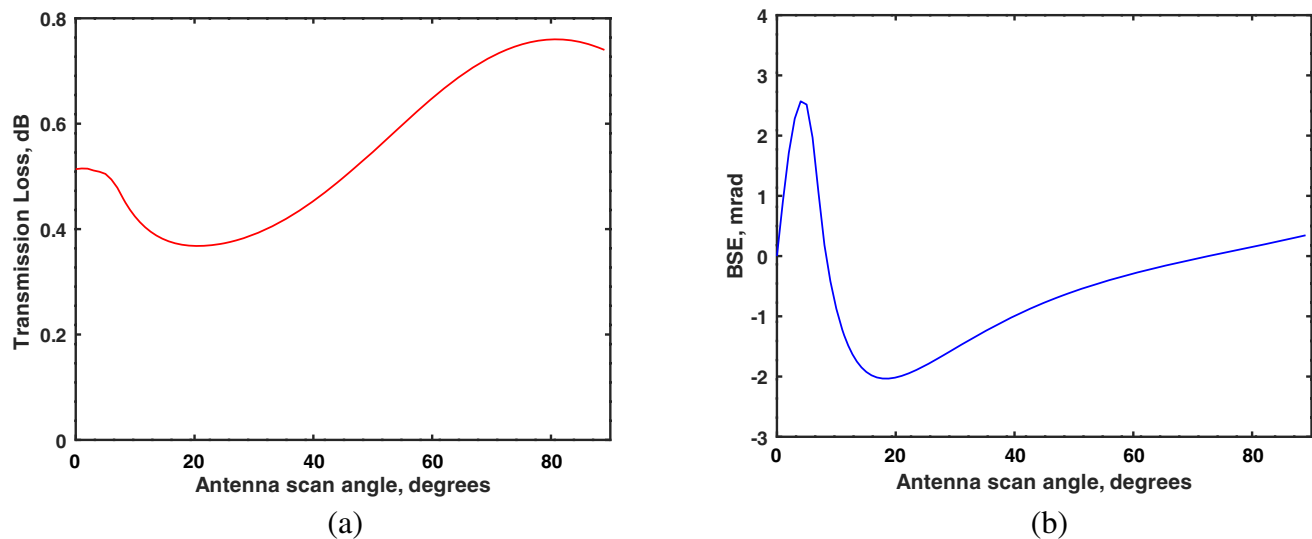


Figure A1. (a) Transmission loss and (b) boresight error of the radome.

REFERENCES

1. Shavit, R., *Radome Electromagnetic Theory and Design*, Wiley Online Library, 2018.
2. Cary, R. J. H., *The Handbook of Antenna Design*, Peter Peregrinus Ltd., 1983.
3. Kozakoff, D. J., *Analysis of Radome-enclosed Antennas*, 2nd Edition, Artech House, 2010.
4. Nair, R., M. Suprava, and R. Jha, "Graded dielectric inhomogeneous streamlined radome for airborne applications," *Electronics Letters*, Vol. 51, No. 11, 862–863, 2015.

5. Yazeen, P. M., C. Vinisha, S. Vandana, M. Suprava, and R. U. Nair, "Electromagnetic performance analysis of graded dielectric inhomogeneous streamlined airborne radome," *IEEE Transactions on Antennas and Propagation*, Vol. 65, No. 5, 2718–2723, 2017.
6. Nair, R. U. and R. M. Jha, "Electromagnetic design and performance analysis of airborne radomes: Trends and perspectives," *IEEE Antennas and Propagation Magazine*, Vol. 56, No. 4, 276–298, 2014.
7. Zhou, L., Y. Pei, and D. Fang, "Dual-band A-sandwich radome design for airborne applications," *IEEE Antennas and Wireless Propagation Letters*, Vol. 15, 218–221, 2015.
8. Xu, W., B. Y. Duan, P. Li, N. Hu, and Y. Qiu, "Multiobjective particle swarm optimization of boresight error and transmission loss for airborne radomes," *IEEE Transactions on Antennas and Propagation*, Vol. 62, No. 11, 5880–5885, 2014.
9. Xu, W., B. Duan, P. Li, and Y. Qiu, "A new efficient thickness profile design method for streamlined airborne radomes," *IEEE Transactions on Antennas and Propagation*, Vol. 65, No. 11, 6190–6195, 2017.
10. Xu, W., B. Duan, P. Li, and Y. Qiu, "Study on the electromagnetic performance of inhomogeneous radomes for airborne applications. Part I: Characteristics of phase distortion and boresight error," *IEEE Transactions on Antennas and Propagation*, Vol. 65, No. 6, 3162–3174, 2017.
11. Xu, W., P. Li, and Y. Qiu, "Electromagnetic performance analysis of inhomogeneous airborne radomes for circular polarization applications," *IEEE Antennas and Wireless Propagation Letters*, Vol. 18, 74–78, 2019.
12. Zhou, L., Y. Pei, R. Zhang, and D. Fang, "Optimal design for high-temperature broadband radome wall with symmetrical graded porous structure," *Progress In Electromagnetics Research*, Vol. 127, 1–14, 2012.
13. Kilcoyne, N. R., "A two-dimensional ray-tracing method for the calculation of radome boresight error and antenna pattern distortion," Ohio State Univ. Columbus Electroscience Lab., 1963.
14. Weckesser, L. B., R. K. Frazer, D. J. Yost, B. E. Kuehne, G. P. Tricoles, R. Hayward, and E. L. Rope, "Aerodynamic heating effects on radome boresight errors," *Proceeding of 14th Symposium on Electromagnetic Windows*, 45–51, 1978.
15. Nair, P. R. U. and R. M. Jha, "Temperature dependent EM performance predictions of dielectric slab based on inhomogeneous planar layer model," *IEEE Antennas and Wireless Propagation Letters*, 1–2, 2012.
16. Sonalikar, H. S., "Temperature dependent EM investigation of inhomogeneous dielectric wall for application in ablatable radome," *2018 IEEE Indian Conference on Antennas and Propagation (InCAP)*, 1–5, Hyderabad, India, December 2018.
17. Aparna, A. P. and H. S. Sonalikar, "Temperature dependent electromagnetic design of dielectric wall for airborne applications," *2019 IEEE Indian Conference on Antennas and Propagation (InCAP)*, Ahmedabad, India, December 2019.
18. Nair, R. U., S. Vandhana, S. Sandhya, and R. M. Jha, "Temperature-dependent electromagnetic performance predictions of a hypersonic streamlined radome," *Progress In Electromagnetics Research*, Vol. 154, 65–78, 2015.
19. Nair, R. U. and R. M. Jha, "Electromagnetic performance analysis of a novel monolithic radome for airborne applications," *IEEE Transactions on Antennas and Propagation*, Vol. 57, 3664–3668, 2009.
20. Crone, G. A. E., A. W. Rudge, and G. N. Taylor, "Design and performance of airborne radomes: A review," *IEE Proc.*, Vol. 128, 451–464, 1981.
21. Rabbath, C. A. and D. Corriveau, "A comparison of piecewise cubic Hermite interpolating polynomials, cubic splines and piecewise linear functions for the approximation of projectile aerodynamics," *Defence Technology*, Vol. 15, No. 5, 741–757, 2019.
22. Chen, F., Q. Shen, and L. Zhang, "Electromagnetic optimal design and preparation of broadband ceramic radome material with graded porous structure," *Progress In Electromagnetics Research*, Vol. 105, 445–461, 2010.

23. Eliason, L. K. and G. C. Zellner, "A survey of high temperature ceramic materials for radomes," Melpar Inc., Falls Church, VA, 1964.
24. Aparna, A. P. and H. S. Sonaliker, "Fast computation of radome EM parameters with golden section search method for radiation pattern peak detection," *Proc. 5th International Conference on Electronics, Computing and Communication Technologies (IEEE CONECCT)*, Bangalore, India, July 2019.
25. Zanwar, Y. S., A. Parameswaran, and H. S. Sonaliker, "Optimization of gimbal parameters to improve the boresight error performance of airborne radomes," *Progress In Electromagnetics Research M*, Vol. 90, 127–135, 2020.
26. Burks, D. G. and J. L. Volakis, "*Radomes*" in *Antenna Engineering Handbook*, McGraw-Hill, 2007.